

Photodissociation regions and star formation in the Carina Nebula

J.M. Rathborne¹, M.G. Burton^{1,2}, K.J. Brooks³, M. Cohen⁴,
M.C.B. Ashley¹, J.W.V. Storey¹

¹*School of Physics, The University of New South Wales, Sydney, NSW, 2052, Australia*

²*School of Cosmic Physics, Dublin Institute for Advanced Studies, 5 Merrion Square, Dublin 2, Ireland*

³*European Southern Observatory, Casilla 19001, Santiago 19, Chile*

⁴*Radio Astronomy Lab, 601 Campbell Hall, University of California, Berkeley, CA 94720, USA*

27 October 2018

ABSTRACT

We have obtained wide-field thermal infrared (IR) images of the Carina Nebula, using the SPIREX/Abu telescope at the South Pole. Emission from poly-cyclic aromatic hydrocarbons (PAHs) at $3.29\mu\text{m}$, a tracer of photodissociation regions (PDRs), reveals many interesting well defined clumps and diffuse regions throughout the complex. Near-IR images ($1\text{--}2\mu\text{m}$), along with images from the Midcourse Space Experiment (*MSX*) satellite ($8\text{--}21\mu\text{m}$) were incorporated to study the interactions between the young stars and the surrounding molecular cloud in more detail. Two new PAH emission clumps have been identified in the Keyhole Nebula and were mapped in $^{12}\text{CO}(2\text{--}1)$ and $(1\text{--}0)$ using the SEST. Analysis of their physical properties reveals they are dense molecular clumps, externally heated with PDRs on their surfaces and supported by external pressure in a similar manner to the other clumps in the region. A previously identified externally heated globule containing IRAS 10430-5931 in the southern molecular cloud, shows strong $3.29\text{--}, 8\text{--},$ and $21\text{--}\mu\text{m}$ emission, the spectral energy distribution (SED) revealing the location of an ultra-compact (UC) H II region. The northern part of the nebula is complicated, with PAH emission inter-mixed with mid-IR dust continuum emission. Several point sources are located here and through a two-component black-body fit to their SEDs, we have identified 3 possible UC H II regions as well as a young star surrounded by a circumstellar disc. This implies that star formation in this region is on-going and not halted by the intense radiation from the surrounding young massive stars.

Key words: H II regions – stars: formation – ISM: lines and bands – ISM: molecules – ISM: structure.

1 INTRODUCTION

The Carina Nebula is an H II region/molecular cloud complex containing some of the most massive star clusters identified in our galaxy. The nebula is at a distance of 2.2 kpc (Tovmassian 1995) and allows us to study the impact young massive stars have on their surroundings and in particular whether they trigger or hinder further star formation. The region is immersed in the UV radiation and stellar winds from the many clusters; Trumpler 14 (Tr 14) and Tr 16 being the most influential. Several O-type stars are found here, including six O3 stars (Walborn 1995) and the spectacular star η Car. Optical images reveal the many interesting aspects of this region including bright-rimmed globules, filaments, dark patches and large dust lanes that bisect the complex. Radio continuum observations reveal a large ion-

ized region with two peaks, Car I and Car II (Gardner & Morimoto 1968). Both of these H II regions contain arc and filamentary structures many of which correspond to optical features. They are consistent with ionization fronts from Tr 14 and Tr 16 respectively (Retallack 1983; Whiteoak 1994; Brooks, Storey & Whiteoak 2001).

Evidence for on-going star formation in the nebula has been scarce, with only one possible site identified (Megeath et al. 1996). Due to the paucity of star formation sites, it was suggested that the massive stars were too destructive on their environment, thus hindering any further star formation (Cox 1995). This view has been recently challenged by results from the Midcourse Space Experiment (*MSX*), revealing several embedded infrared (IR) sources where star formation may be active (Smith et al. 2000). In addition,

Brooks et al. (2001) have identified two compact H II regions possibly corresponding to very young O-type stars.

Recent results from the Short Wavelength Spectrometer (SWS) on-board the Infrared Space Observatory (ISO) in the vicinity of the Car I H II region, reveal a “broad 22- μm ” feature extending from 18–28 μm (Chan & Onaka 2000). This feature has also been reported in the M17-H II region (Jones et al. 1999), and is similar to an emission band attributed to freshly formed dust in ejecta from Cas A (Arendt, Dwek, & Moseley 1999). The spatial variations in intensity with respect to the distance from the Car I emission peak suggests heating of interstellar dust. Arendt et al. (1999) propose the broad 22- μm feature arise from Mg protosilicate grains.

Two distinct regions of CO emission have been identified in the Carina Nebula (de Graauw et al. 1981; Whiteoak & Otrupcek 1984; Brooks, Whiteoak & Storey 1998). Large-scale studies have found these are part of a much larger giant molecular cloud (GMC). The two regions, referred to as the northern and southern clouds, are elongated over 130 pc and contain a mass in excess of $5 \times 10^5 M_{\odot}$ (Grabelsky et al. 1988). Between them lies the Keyhole Nebula, consisting of many discrete molecular clumps with masses of $\sim 10 M_{\odot}$ (Cox & Bronfman 1995). Little is known about the extent of the interaction between the stars and molecular material. The far-UV (FUV) radiation from massive stars penetrates through an inhomogeneous GMC and dominates the heating and chemistry of the gas. This occurs at interface regions where the molecular material is directly exposed, resulting in photo-dissociation regions (PDRs; Hollenbach & Tielens 1999). Under this premise we would expect PDRs to be prominent throughout the Carina Nebula.

Poly-cyclic aromatic hydrocarbon (PAH) molecules are excellent tracers of PDRs. Emission from PAH molecules is widespread in many astrophysical environments (Cohen et al. 1986; Allamandola, Tielens, & Barker 1989; Cohen et al. 1989). PAH molecules are excited by FUV radiation and emit fluorescently in several IR bands (often referred to as the Aromatic Infrared Bands, AIBs). The main features which occur at 3.3, 6.2, 7.7, 8.6 and 11.3 μm are thought to arise from various bending and stretching modes of PAH molecules (Léger & Puget 1984; Allamandola, Tielens, & Barker 1985; Geballe et al. 1994; Joblin et al. 1995). As well as displaying strong IR emission features, continuum emission from 1–5 μm has also been found in association with these molecules (Sellgren, Werner, & Dinerstein 1983). Recent results from ISO have contributed to advances in modelling PAH cation emission (see review by Verstraete et al. 2001), including the discovery of a new feature at 16.4 μm (Moutou et al. 2000).

Our objective in this paper is to use the band emission from PAH molecules in the Carina Nebula to study the impact of the FUV radiation from the massive stars on the surrounding molecular material. To do this we obtained both high-resolution and wide-field images in the thermal IR of a large region across the Carina Nebula. These images were combined with near- and mid-IR images and with results from follow-up molecular line observations.

2 OBSERVATIONS

2.1 Thermal Infrared: 3–4 μm

Observations were obtained across the Carina Nebula using the South Pole Infra-Red EXplorer (SPIREX) during 1999. SPIREX was a 60-cm telescope built and operated at the South Pole from 1994 to 1999 (Hereld et al. 1990). It was equipped in 1998 with the NOAO Abu IR camera (Fowler et al. 1998), which incorporated an engineering grade 1024 \times 1024 ‘Aladdin’ InSb 1–5 μm array. This produced circular images of approximately 10 arcmin diameter, with a 0.6 arcsec pixel scale.

The Carina region was imaged using two filters, a narrow-band PAH filter centred on 3.29 μm (half-power width of 0.074 μm) and a continuum L-band filter centred on 3.5 μm (half-power width of 0.618 μm). Five overlapping positions across the centre of the nebula were obtained in both these bands. Integration times of 60 s and 6 s were used for individual frames respectively. The observing sequence in all cases consisted of a set of sky frames followed by two sets of object frames. Each set included a 5-point cross, with each frame offset slightly from the previous.

All data reduction was achieved using IRAF^{*}, with archived images used for dark subtraction and flat-fielding. Sky-subtraction was performed using the 6 frames nearest in time to the object frame (regardless of the actual image type). All frames covering the same region were then registered and combined to form the final image. Common stars in adjacent frames were used to match the overlapping regions to produce a larger mosaic. All registering and combining of the individual frames and of the final mosaic were achieved using routines written by McGregor (1995). A coordinate axis was added using a corresponding image obtained with the Digitised Sky Survey[†] (DSS) and the program KOORDS (Gooch 1996).

For the PAH-band a total of 72 individual frames were used to produce the final mosaiced image. This image contains both line and continuum emission. The amount of continuum contribution in the PAH band was estimated using the L-band images and vice-versa for contamination to the continuum fluxes from PAH molecules. This contamination was removed from the PAH emission and L-band continuum flux values given for each source.

Observations of the standard star, HR 4638, using both the PAH- and L-band filters, were used for flux calibration (B3V star, L-band magnitude of 4.50 mag). Based on the repeatability of the standard over the observing periods, we estimate the PAH fluxes to have an uncertainty of ± 9 per cent, with an uncertainty of ± 20 per cent for the L-band fluxes. The L-band fluxes are more uncertain due to poorer weather conditions and tracking during the observations. The diffraction limit at 3.3 μm of the telescope is 1.4 arcsec, comparable to the typical ice-level seeing of the site. However, a combination of tracking errors, tower shake and co-addition of frames limited the stellar FWHM for the PAH images to 2.8 arcsec. The final PAH image has a 1 σ rms noise of $4 \times 10^{-15} \text{ erg s}^{-1} \text{ cm}^{-2} \text{ pixel}^{-1}$.

^{*} IRAF is the Image Reduction and Analysis Facility written and supported by NOAO, see <http://iraf.noao.edu/>

[†] see <http://archive.stsci.edu/dss>

2.2 Mid Infrared: 8–21 μm

Degree-scale images from 8–21 μm were obtained toward the Carina region from the *MSX* satellite[‡] and covered four discrete bandpasses; Band A (6.8–10.8 μm , hereafter referred to as the 8- μm band), Band C (11.1–13.2 μm), Band D (13.5–15.9 μm) and Band E (18.2–25.1 μm , hereafter referred to as the 21- μm band). These images reveal a great deal of information about the interaction and physical conditions of the material in this region. Emission seen in the 21- μm band arises from warm dust at ~ 100 K, and is used to identify deeply embedded sources. The 22- μm feature identified by Chan & Onaka (2000) contributes ~ 15 –30 per cent of the flux in the 21- μm band. This was estimated using their Figs. 1 and 2, in which the spectra represent the position where the feature appears the strongest.

The 8- μm band is more complex, including several discrete PAH emission features, the plateau of emission from 6–9 μm as well as emission from dust at ~ 400 K. It is not possible to determine which process causes the observed emission from this band alone. By using it in combination with the 3.29- and 21- μm emission structures, it is possible to identify regions where the 8- μm emission is coming from PAH molecules and where it arises from warm dust. In general, where the 3.29- and 8- μm emission are spatially well-correlated we attribute the emission dominantly to that from PAHs. If the 8- and 21- μm emission are spatially well-matched, however, the emission is dominated by continuum emission.

2.3 Near Infrared: 1–2 μm

Bright extended emission detected in the SPIREX/Abu images toward the southern Carina region and several point sources located further north were observed using the Australian National University 2.3-m telescope at Siding Spring Observatory, Australia. The Near-IR camera CASPIR (Cryogenic Array Spectrometer Imager; McGregor et al. 1994) contains a 256×256 InSb array and was used to image J (1.25 μm), H (1.65 μm) and K (2.2 μm) bands during 2000 June. Individual images cover approximately 2×2 arcmin² (0.5 arcsec pixel scale) with integration times of 5 s for J- and H-band and 2 s for K-band images. Standard stars were observed before each set of image frames.

Data reduction was achieved using CASPIR specific routines within IRAF (McGregor 1995). Images were dark- and bias-subtracted, before linearisation and flat-fielding were performed. Sky background was removed by averaging the sky value obtained over several consecutive image frames. Coordinates were applied using a corresponding image from the DSS and the program KOORDS.

2.4 Millimetre

Two new PAH emission structures located in the Keyhole region were identified from the images obtained with SPIREX/Abu. Observations of $^{12}\text{CO}(1-0)$ at 115.271 GHz

and $^{12}\text{CO}(2-1)$ at 230.537 GHz were obtained toward these structures during 2000 October using the 15-m Swedish-ESO Submillimetre Telescope (SEST)[§] at La Silla Observatory, Chile. Both transitions were observed simultaneously with the IRAM-built 230/115 GHz SIS receiver tuned to single side-band (SSB) mode and connected to a narrow-band (43 MHz) Acousto-Optical Spectrometer (AOS) with a channel resolution of 0.08 MHz. This corresponds to approximately 0.1 km s^{-1} at 115 GHz and 0.05 km s^{-1} at 230 GHz. The bands were centred on a radial velocity of -10 km s^{-1} with respect to the local standard of rest (LSR) for one emission structure and -5 km s^{-1} for the other. Position-switching mode was used with η Car used as the signal-free reference position. An integration time of 60 s was used for all observations. The average system temperatures during the observations were ~ 200 K for the 115 GHz band and ~ 400 K for the 230 GHz band. Chopper-wheel calibration was performed every 10 mins to obtain atmosphere-corrected antenna temperatures according to the method described by Ulich & Haas (1976). The telescope pointing and sub-reflector focusing were checked regularly using suitably bright nearby SiO masers. We estimate the pointing accuracy to be better than 10 arcsec and adopt the standard SEST value of 10 per cent uncertainty in the temperature scale. The beam size of the SEST is 45 arcsec at 115 GHz and 22 arcsec at 230 GHz.

Observations toward both PAH structures were obtained using a 20 arcsec pointing grid, covering areas of $\sim 4 \times 4$ arcmin² and $\sim 3 \times 3$ arcmin² for each region. These regions were centred on the peak in the PAH emission.

All spectra were processed using GILDAS software (Buisson et al. 1999). Linear baselines were initially removed from each spectra and the temperature scale converted to main-beam brightness temperature using the values for the main beam efficiencies of 0.7 for 115 GHz and 0.5 for 230 GHz. The $^{12}\text{CO}(1-0)$ data were smoothed to a 40 arcsec grid to match the beam size of the SEST at 115 GHz. The average rms noise per spectral channel was 0.8 K for both $^{12}\text{CO}(1-0)$ and $^{12}\text{CO}(2-1)$.

3 RESULTS AND DISCUSSION

3.1 The Carina Nebula in 3.29- μm emission

Fig. 1 shows the 3.29- μm emission observed across the Carina Nebula. The emission can be grouped into three main regions identified as: Keyhole region, southern region and northern region. The peak position, peak intensity, size and total integrated intensity of the structures within these three regions are given in Table 1. The contamination from continuum emission was estimated and subtracted from the total flux seen toward each region. Thus, the flux values given in Table 1 are estimates of the contribution to the emission from the 3.29- μm PAH line only. The extended emission seen throughout Fig. 1 is predominantly from the 3.29- μm PAH emission line, with the majority of the continuum emission contained in the point sources.

[‡] For a full description of the *MSX* satellite, the astrophysical experiments and the observing techniques see Mill et al. (1994), Price et al. (1996), Egan et al. (1998) and Price et al. (2001).

[§] The SEST is operated jointly by ESO and the Swedish National Facility for Radio Astronomy, Onsala Space Observatory, Chalmers University of Technology.

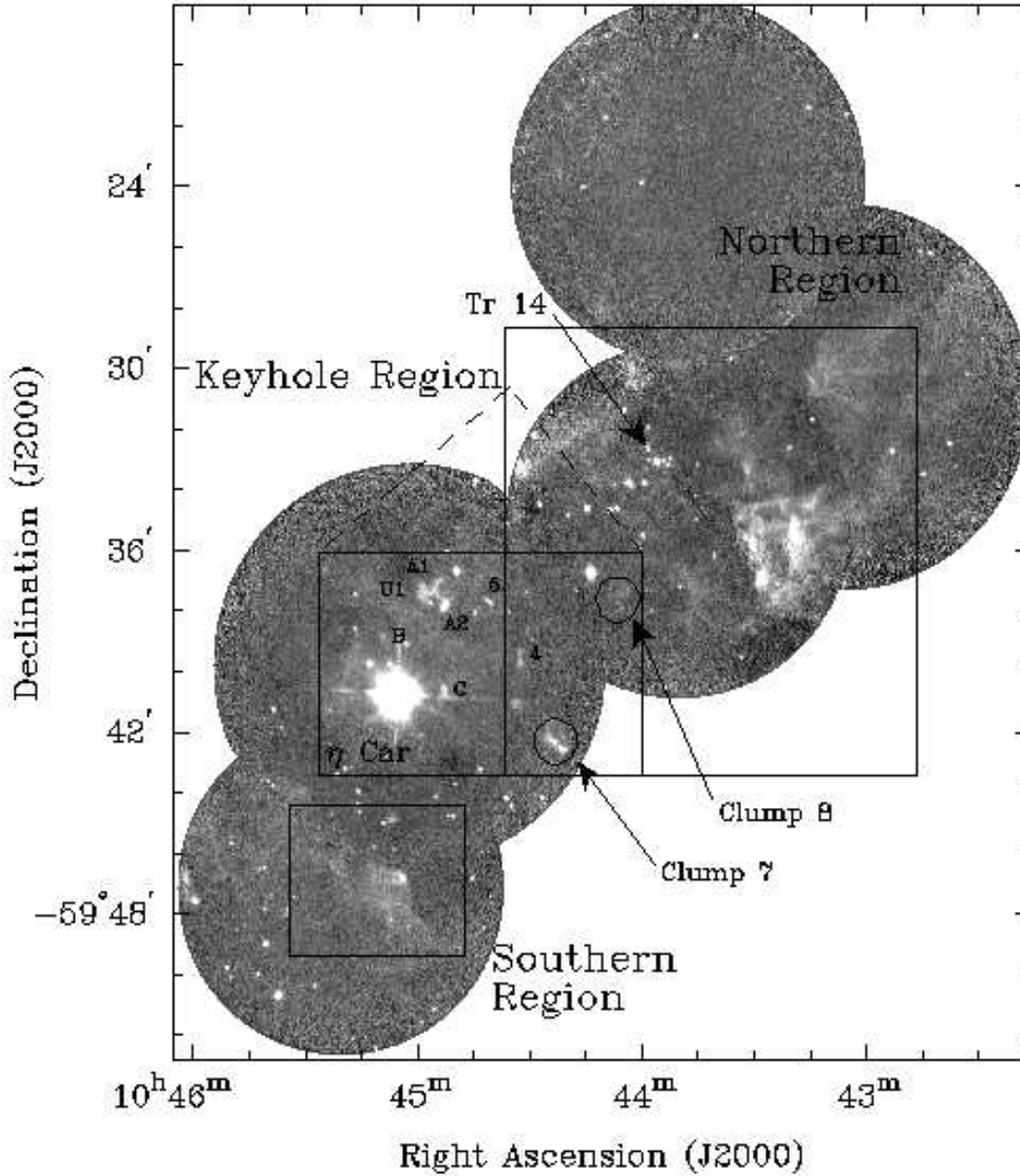


Figure 1. The Carina Region in the 3.29- μm PAH and continuum emission. The cluster Tr 14 is apparent along with the massive star η Car. Clumps of emission within the Keyhole region are labelled along with the regions (outlined by boxes) discussed in more detail in the following sections.

Table 1. Measured 3.29- μm PAH emission parameters for the regions shown in Fig. 1. These represent continuum corrected fluxes^a.

Region	Peak position		Peak Intensity ^b	Size	Integrated Intensity
	RA	DEC	($\times 10^{-14}$ erg s ⁻¹ cm ⁻² arcsec ⁻²)	" \times "	($\times 10^{-11}$ erg s ⁻¹ cm ⁻²)
	(2000)	(2000)			
Clump 7	10 44 23	-59 42 14	7.1	90 \times 60	4.0
Clump 8	10 44 06	-59 37 21	3.4	60 \times 100	2.9
Southern region	10 45 00	-59 47 03	5.1	300 \times 120	3.1
Northern region	10 43 20	-59 34 53	35	450 \times 240	97

^a The contamination to the total fluxes from continuum emission was estimated to be 10 per cent for clump 7 and the Northern region, 20 per cent for the Southern region and less than 1 per cent for clump 8.

^b 1 σ rms noise of 1×10^{-14} erg s⁻¹ cm⁻² arcsec⁻²

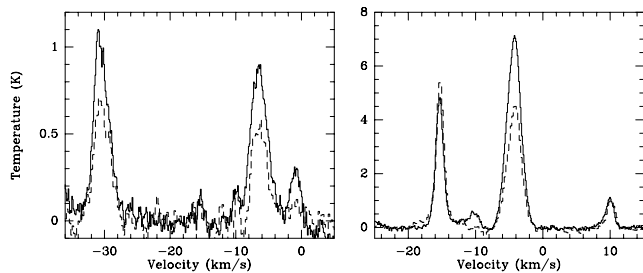


Figure 2. The averaged line profiles for all positions observed toward clumps 7 (left) and 8 (right). The solid line refers to the $^{12}\text{CO}(2-1)$, while the dashed line represents the $(1-0)$ emission.

The region situated at the centre of Fig. 1 includes the Keyhole Nebula and η Car. Previous studies of these sources have shown they are dense molecular clumps (Cox & Bronfman 1995) which, in addition to bright $3.29\text{-}\mu\text{m}$ PAH emission, exhibit strong H_2 ($2.12\text{-}\mu\text{m}$) emission (Brooks et al. 2000). The coincidence between these features is indicative of the existence of PDRs on the clumps' surfaces. The larger area covered in our study reveals two additional $3.29\text{-}\mu\text{m}$ emission structures. One is located in the south-western corner of the Keyhole region, while the other is much fainter and is displaced further toward Tr 14. This region will be discussed in more detail in section 3.2.

In contrast to the Keyhole region, the $3.29\text{-}\mu\text{m}$ emission detected in the southern region is much more diffuse. The extent of the emission here traces the sharp northern rim of the southern molecular cloud. Several *IRAS* sources are located along the edge of this molecular cloud. The peak seen in $3.29\text{-}\mu\text{m}$ emission corresponds to one such source, IRAS 10430-5931, and is the location of a bright-rimmed globule identified through a combination of molecular line and IR observations (Megeath et al. 1996). The structures seen in this region will be discussed further in section 3.3.

The northern region reveals a similar environment to that seen in the south, with extended diffuse emission covering the whole region. The brightest $3.29\text{-}\mu\text{m}$ emission is located to the west of the cluster Tr 14 and follows the sharp edge of the northern molecular cloud. This edge corresponds to a dark obscuring region in optical images. The second peak in the $3.29\text{-}\mu\text{m}$ emission is located further to the west. The extent of the emission in this region is coincident with the edge of the ionization peak Car I, confirming the existence of a PDR at the interface between the ionized and molecular material. The peak intensity of the emission here is almost 10 times higher than the other regions observed (see Table 1). The close proximity of the cluster to the molecular material offers an ideal location in which to study their interaction. The northern molecular cloud extends much further to the north of this region than is indicated by the $3.29\text{-}\mu\text{m}$ emission. The absence of any emission to the north may be a consequence of a weaker FUV radiation field. The northern region will be discussed in more detail in section 3.4.

From the $3.29\text{-}\mu\text{m}$ emission seen in Fig. 1 it is clear that PDRs extend across the whole Carina GMC. The emission we see is not limited to the vicinity of a single source, but penetrates through the whole region and interacts with the molecular material across the complex. This is facil-

Table 2. Properties of the $^{12}\text{CO}(2-1)$ and $(1-0)$ profiles seen toward clumps 7 and 8. These values are obtained from Gaussian fits to the profiles shown in Fig. 2, where ΔV represents the FWHM estimate for the profiles.

$^{12}\text{CO}(1-0)$			$^{12}\text{CO}(2-1)$		
Velocity km s^{-1}	Peak K	ΔV km s^{-1}	Velocity km s^{-1}	Peak K	ΔV km s^{-1}
Clump 7					
-30.4	0.7	2.8	-30.5	1.0	2.8
-15.8	0.1	1.4	-15.4	0.2	0.9
-9.8	0.2	0.5	-10.0	0.2	0.9
-6.3	0.6	2.5	-6.5	0.9	3.0
-1.0	0.1	1.0	-0.9	0.3	1.6
Clump 8					
-15.3	5.2	1.4	-15.3	4.7	1.4
			-10.4	0.7	1.5
-4.2	4.4	2.4	-4.3	7.0	2.5
10.1	1.0	1.4	9.9	1.1	1.4

itated by the inhomogeneous nature of the region and is a common characteristic of star forming regions, including NGC 6334 (Burton et al. 2000), the Rosette (Schneider et al. 1998), M17 (Stutzki et al. 1988; Meixner et al. 1992), Orion (Tauber et al. 1995) and W51 (Genzel et al. 1988).

3.2 Keyhole region

The molecular clumps of this region are typically 10-30 arcsec in length and all correspond to striking optical features such as dark patches, some with bright rims. Their mass is of order $10 M_{\odot}$, they are gravitationally bound and emit over a velocity from 0 to -30 km s^{-1} (LSR) (Cox & Bronfman 1995).

3.2.1 New molecular clumps

In this section we consider the results of the molecular line maps around the two new $3.29\text{-}\mu\text{m}$ PAH emission structures, in order to determine if these new sources are in fact molecular clumps with PDRs on their surfaces.

Fig. 2 shows the $^{12}\text{CO}(2-1)$ and $(1-0)$ line profiles, averaged over the two regions (hereafter referred to as clumps 7 and 8). It is clear from the spectra that emission from separate velocity ranges exists toward both of these regions. The peak temperature, velocity and FWHM were determined from Gaussian fits to each feature and are listed in Table 2.

From the emission seen toward clump 7, five $^{12}\text{CO}(2-1)$ profiles can be identified of which the strongest and most distinct occur over the ranges -34 to -26 km s^{-1} , -9 to -2 km s^{-1} and -2 to 2 km s^{-1} . Maps of the integrated $^{12}\text{CO}(2-1)$ emission over each of these velocity ranges are shown in Fig. 3(a). The velocity range -30 to -20 km s^{-1} corresponds to that of the southern molecular cloud (Brooks et al. 1998). The emission in the range -34 to -26 km s^{-1} is spatially coincident with the edge of this cloud. The emission between -9 to -2 km s^{-1} is located further eastwards and corresponds to a faint nebulous patch in optical images. The location and morphology of this feature matches with the $3.29\text{-}\mu\text{m}$ PAH emission (Fig. 4(a)). The final component, in the range -2 to 2 km s^{-1} , has much

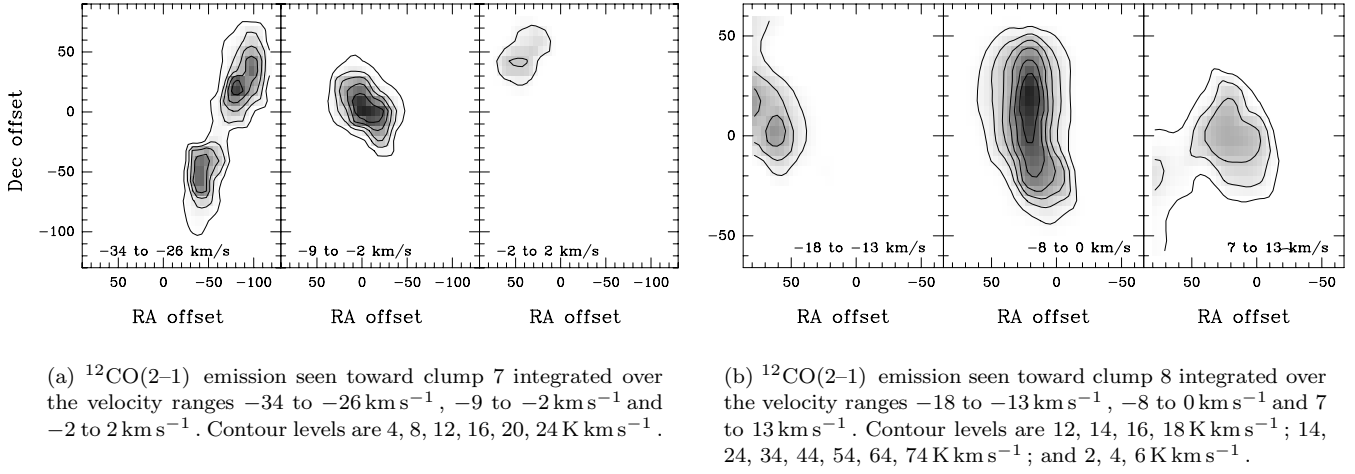


Figure 3. Integrated intensity of the $^{12}\text{CO}(2-1)$ emission seen toward the two new $3.29\text{-}\mu\text{m}$ PAH emission structures identified in the Keyhole region. The offsets are relative to the $3.29\text{-}\mu\text{m}$ emission peaks given in Table 1.

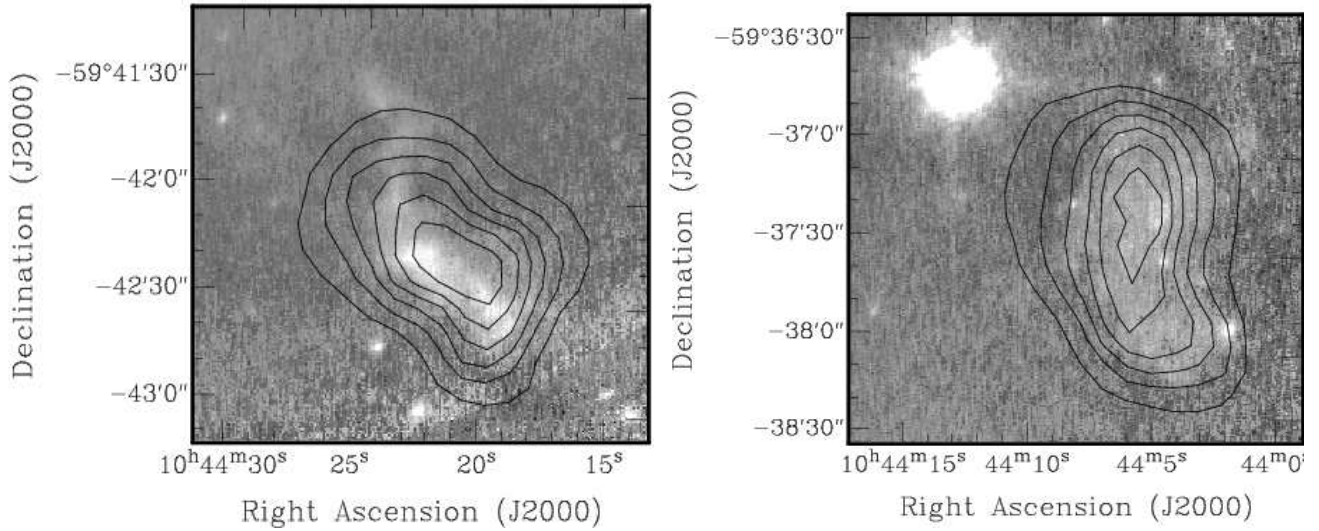


Figure 4. $3.29\text{-}\mu\text{m}$ emission from the two new clumps identified, overlaid with the corresponding $^{12}\text{CO}(2-1)$ emission. Several stars are also evident in these images, in particular at the north east edge in (b).

Table 3. The physical properties of the clumps 7 and 8 in the Keyhole region, estimated from values obtained from Gaussian fits to the averaged spectra over the regions enclosed by the clumps, as seen in Fig. 5. The LTE mass is estimated from local thermal equilibrium conditions. The ratio calculated is for the ^{12}CO integrated fluxes, with $n(\text{H}_2)$ representing the average H_2 density and ΔV representing the FWHM of the profile.

Clump	$^{12}\text{CO}(1-0)$			$^{12}\text{CO}(2-1)$			Ratio 2-1/1-0	Area deg^2	Mass		$n(\text{H}_2)$ cm^{-3}
	Velocity km s^{-1}	Peak K	ΔV km s^{-1}	Velocity km s^{-1}	Peak K	ΔV km s^{-1}			LTE M_\odot	Virial M_\odot	
7	-6.6	1.0	2.9	-6.6	2.1	3.2	2.4	4.2×10^{-4}	12	417	0.7×10^3
8	-4.0	7.0	2.8	-4.2	10.4	2.1	1.1	4.6×10^{-4}	91	411	4.5×10^3

fainter molecular emission, with no obvious counterpart in optical images of the region.

For the emission seen toward clump 8, four profiles are evident, the strongest of these occurring over the ranges -18 to -13 km s^{-1} , -8 to 0 km s^{-1} and 7 to 13 km s^{-1} . Fig. 3(b) shows the integrated emission over the velocity ranges seen toward this region. The velocity range -20 to 0 km s^{-1} corresponds to the back face of the northern molecular cloud (Brooks 2000). The emission between -18 to -13 km s^{-1} corresponds the edge of a larger component that extends further northwards and eastwards. The emission we see here coincides with bright diffuse emission in optical images and is most likely from the H II region in the northern molecular cloud. The emission between -8 to 0 km s^{-1} traces an isolated feature that coincides with the detected $3.29\text{-}\mu\text{m}$ PAH emission (see Fig. 4(b)) and also to a dark optical region. The feature seen in the velocity range 7 to 13 km s^{-1} extends further to the east, with considerably fainter emission and no obvious optical counterpart.

Therefore, the two new $3.29\text{-}\mu\text{m}$ PAH structures (7 and 8) are consistent with dense molecular clumps at velocities of -6.3 km s^{-1} and -4.2 km s^{-1} . The other CO emission features seen here are most likely foreground and background objects seen along the line of sight, the only common features being those at -10 km s^{-1} and -15 km s^{-1} , suggesting these may be much larger structures not associated with the Carina Nebula.

3.2.2 Physical properties of the new clumps

This section considers the physical conditions within the Keyhole region and the subsequent exposure of the molecular material. The characteristics of the emission seen will determine if the new clumps identified here are influenced in a similar way to the other clumps in the region. To achieve this the spectral profiles contained within the region enclosed by the clumps were averaged (Fig. 5). The results of Gaussian fits to these profiles are given in Table 3, along with the $^{12}\text{CO}(2-1)$ and $(1-0)$ integrated line ratio, mass estimates and average H_2 densities.

For clump 7 the $^{12}\text{CO}(2-1)$ and $(1-0)$ line ratio was found to be ~ 2 , while for clump 8 it was closer to 1. Ratios greater than unity are typically found in regions where the cloud is warm ($T_k \geq 40 \text{ K}$), with average H_2 densities $n(\text{H}_2) > 1 \times 10^3 \text{ cm}^{-3}$ and optically thick ($\tau_{21} > 5$) (Sakamoto et al. 1994). This ratio is seen in many star-forming regions including Orion, the Rosette complex and M17 (Castets et al. 1990; Sakamoto et al. 1994; Hasegawa 1996) and is explained in terms of the external heating of molecular material from FUV radiation.

Estimates of the local thermal equilibrium (LTE) and Virial masses were obtained for each of the clumps. The LTE mass was calculated under the assumption that the H_2 column density ($N(\text{H}_2)$) is proportional to the integrated intensity of the $^{12}\text{CO}(1-0)$ line. Using the constant of proportionality of $3 \times 10^{20} (\text{K km s}^{-1})^{-1}$ (Scoville et al. 1991) and assuming a distance to the clumps of 2.2 kpc , we estimate values of $12 M_\odot$ and $91 M_\odot$ for the clumps 7 and 8 respectively. Calculations for the Virial mass assume that the velocity width of the CO line is a measure of the motion of the overall gas and therefore the mass. Values obtained for the Virial mass are significantly greater than those cal-

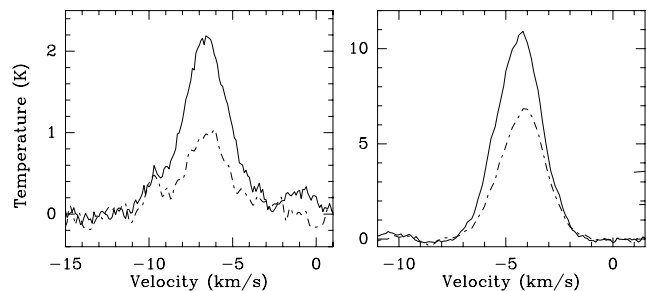


Figure 5. The averaged spectra for the regions enclosed by each of the structures; clump 7 (left) and clump 8 (right). The solid line represents $^{12}\text{CO}(2-1)$ emission, while the dashed line represents $^{12}\text{CO}(1-0)$ emission. Results of Gaussian fits to these profiles are given in Table 3.

culated for the LTE mass, even considering that the LTE values may be under-estimated by a factor of 3. This implies that the clumps are probably not gravitationally bound and instead are supported by external pressure. This is consistent with the other clumps in the region.

Brooks et al. (2000) have developed a geometrical model for the Keyhole region whereby clumps with velocities of -28 km s^{-1} and more negative are dark obscuring regions in front of the nebula; clumps with velocities in the range -25 to -17 km s^{-1} are inside the nebula and have bright rims in optical images; and clumps with velocities of -9 km s^{-1} and more positive are behind the nebula and correspond to faint optical patches. From our results we see that the two new clumps with velocities of -6 km s^{-1} and -4 km s^{-1} both correspond to dark regions in optical images. According to the above model, this places them at the back of the nebula.

Estimations of the winds and radiation from the massive stars in particular η Car suggest the clumps are photo-evaporating and represent the swept up remains of the natal cloud from which the stars formed (Cox & Bronfman 1995; Brooks et al. 2000). The two new clumps identified here support this view although their larger size and higher PAH fluxes suggest the photo-evaporation process may be slower. This is consistent with η Car being the most influential source, their larger displacement from it most likely reducing the severity of the interaction.

3.2.3 Mid-IR emission in the Keyhole region

Due to the resolution of the *MSX* images and the fact that η Car is an extremely strong mid-IR source, a study of the Keyhole region is difficult using these data. Fig. 6 shows $3.29\text{-}\mu\text{m}$ and $8\text{-}\mu\text{m}$ emission seen toward clumps A1, A2, 5 and 7. All of these clumps are located far enough from η Car to be detected above scattered emission from η Car. Clump 8 is not included however as the mid-IR emission is too faint to be distinguished from the many other sources.

In all cases, the clumps show a strong coincidence between the $3.29\text{-}\mu\text{m}$ and $8\text{-}\mu\text{m}$ emission, confirming the $8\text{-}\mu\text{m}$ emission detected here is dominated by PAH emission. Clump A2 is the only case where $21\text{-}\mu\text{m}$ emission is found above the background and associated with a known feature. The $21\text{-}\mu\text{m}$ emission seen toward this clump is faint and slightly offset from the peaks of the $3.29\text{-}\mu\text{m}$ and $8\text{-}\mu\text{m}$ emission and may not be associated directly with clump A2. Instead

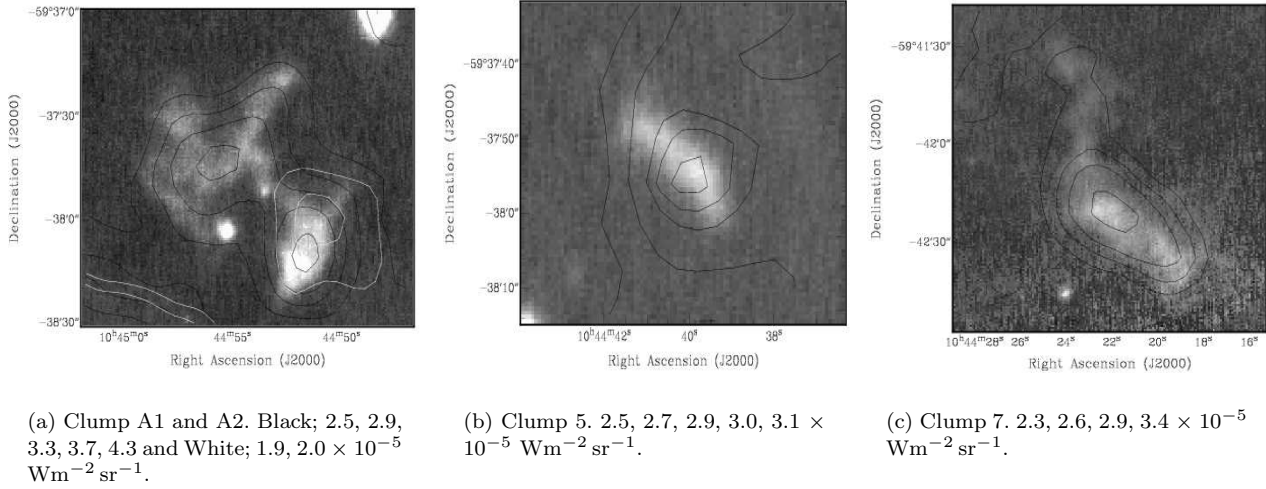


Figure 6. 3.29- μm emission in grey scale overlaid with 8- μm emission (black contours) seen toward several of the molecular clumps identified in the Keyhole region. Clump A2 also shows 21- μm emission (white contours) coincident with it.

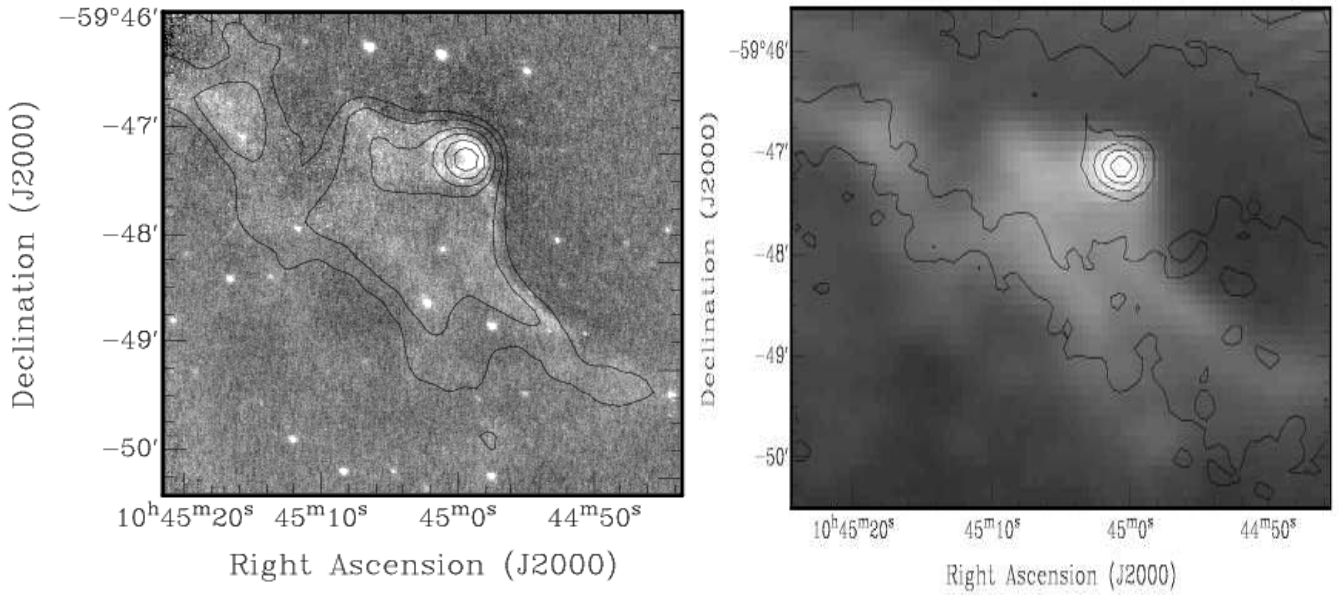


Figure 7. The Southern Carina region. These images cover the same region as indicated in Fig. 1.

the feature may be associated with cooler dust belonging to clump 1 of Cox & Bronfman (1995). This molecular clump overlaps spatially with clump A2 and is distinguishable via its more negative velocity (-34 km s^{-1}). In the model by Brooks et al. (2000) clumps 1, 2 and 3 (which correspond to the actual keyhole obscuring features seen at optical wavelengths) are situated in front of the nebula. They show no signs of PDR emission and are therefore thought to be less exposed to the radiation field coming from Tr 16.

3.3 Southern region

Fig. 7(a) shows 3.29- μm emission in grey scale with contours of 8- μm emission seen toward the southern region outlined in Fig. 1. The 3.29- μm emission shows a strong source superposed on the extended emission associated with the edge of the large molecular cloud. The same is true for the 8- μm emission suggesting that the emission is from PAHs. The brightest emission is coincident with the previously mentioned bright-rimmed molecular globule and in particular the source IRAS 10430-5931. This is a fairly faint *IRAS* ob-

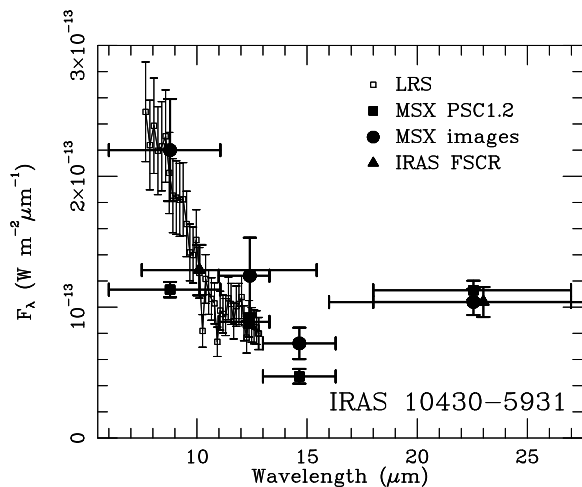


Figure 8. The IRAS LRS spectrum (from 7–13 μm only) of IRAS 10430-5931 (open squares) with $\pm 1\sigma$ error bars. Plotted over the spectrum are the IRAS FSCR (filled triangles) and *MSX* PSC1.2 photometry points (filled squares), together with the results of spatial integrations of the source in the *MSX* images (filled circles). All flux densities are plotted at the isophotal wavelengths appropriate to the source spectrum.

ject with only a 12- μm upper limit in the *IRAS* Point Point Source Catalog. However, the *IRAS* Faint Source Catalog Reject file (FSCR) gives $S_\nu(12\mu\text{m}) = 6 \text{ Jy}$ (± 15 per cent) and $S_\nu(25\mu\text{m}) = 20 \text{ Jy}$ (± 11 per cent). The corresponding 21- μm emission for this region is shown as contours in Fig. 7(b). The source is a bright, compact source at 21- μm , making this the only site in the southern molecular cloud where there is a coincidence between an *IRAS* source, 3.29- and 8- μm emission and a compact 21- μm source.

3.3.1 *IRAS* LRS spectrum for the southern globule

To investigate the character of the diffuse and point source emission further, we have sought *IRAS* Low Resolution Spectrum (LRS) data. Three independent scans were extracted, averaged, recalibrated and normalised (as outlined in Cohen, Walker, & Witteborn 1992) to form the spectra shown in Fig. 8. Unfortunately the long-wavelength part of the spectra contain no valid data hence only the LRS data between 7 and 13 μm are plotted here. Superposed on this spectrum are the flux densities of IRAS 10430-5931 from the FSCR, the point source MSX5C.G287.6393-00.7209 from the *MSX* Point Source Catalogue (PSC1.2) and those that result from spatially integrating the corresponding diffuse peaks in the *MSX* images. The inclusion of these data sets allows us to resolve the point sources (as seen by the smaller *MSX* beam) from the extended emission (as seen by the larger beams of the FSCR and LRS).

There are substantial differences between the point-source and the spatially integrated flux densities in the 8- and 12- μm bands. A modest difference occurs at 14 μm , with a good agreement between the pair of 21- μm flux densities. These confirm our suspicion that the diffuse contributions are chiefly due to emission from PAHs. On the larger spatial scale, the *IRAS* 12- and 25- μm flux densities agree well with those of the LRS spectrum, as do the *MSX* diffuse measure-

ments (the larger uncertainties with the latter are associated with the subtraction of the sky background).

The LRS appears to show a noisy PAH spectrum with a strong 7.7- μm band (defining the blue side of the spectrum), a marginal shoulder of emission near 8.7 μm with no obvious fine structure emission lines. The steepness of the decline between 7.7 and 13 μm rules out a stellar origin as it falls significantly faster than even the Rayleigh-Jeans domain in a cool stellar spectrum and lacks any photospheric absorptions. No obvious 10- μm silicate absorption is seen, and the energy distributions of both the *MSX* point source and spatial integrations suggest thermal emission by cool dust grains. The PAH feature at 11.3 μm is not obvious in the LRS spectrum due to noisy data near 11 μm . However, its presence in the integrated diffuse *MSX* emission is reasonably clear. In H II regions, one expects the intensity ratio of the 11.3- μm band to that of the powerful 7.7- μm band to be ~ 0.29 (Cohen et al. 1986, 1989), but with a range spanning over an order of magnitude among individual objects. Similarly, from the ratio of the 3.3- to 11.3- μm PAH features (~ 2.2 ; Cohen et al. (1986)), we can estimate the expected peak intensity of the 11.3- μm band. Both these estimates indicate $\sim 4 \times 10^{-14} \text{ W m}^{-2} \mu\text{m}^{-1}$, an amount that could well be lost in the noise.

Therefore, we deduce that IRAS 10430-5931 has a compact component which dominates the LRS spectrum but, blueward of $\sim 13 \mu\text{m}$, bright PAH emission bands selectively arise in the surrounding diffuse nebulosity. The excellent agreement between the *IRAS* 25- μm measurement and both *MSX* point-source and spatially integrated data suggests that longward of $\sim 13 \mu\text{m}$, there is only a pointlike source. We also note that the peak emission for all 4 *MSX* bands in the IRAS 10430-5931 region occurs within one pixel of its neighbour, indicating a common point source (presumably the embedded star) with no evidence for any unusually spatially-extended emission at 21- μm . Without the long-wavelength LRS data we have no independent spectroscopy to offer but the accord of *MSX* and *IRAS* points near 23 μm rule out the presence of a broad 22- μm emission line feature of the type found toward Car I by Chan & Onaka (2000).

3.3.2 *SED* for the southern globule

Megeath et al. (1996) found the southern bright-rimmed globule to have a velocity of -27 km s^{-1} , a mass of $67 M_\odot$ and to be gravitationally bound. Also identified near the centre of the globule were four sources displaying anomalous near-IR colours, suggestive of deeply embedded pre-main sequence stars. To determine which of these corresponded to the 8- and 21- μm sources, our own K-band images were used. From Fig. 9 it is clear that the 8- and 21- μm emission peaks correspond to a strong K-band source. This location corresponds to two of the four sources identified by Megeath et al. (1996) (sources 1 and 3). They are separated by less than 2 arcsec and are therefore unresolved in the K-band image. The resolution of the *MSX* images also makes differentiating between these sources difficult.

Fig. 10 shows the Spectral Energy Distribution (SED) for the globule. Included in this plot are fluxes from the *IRAS* HIRAS catalogue for IRAS 10430-5931, fluxes from the *MSX* PSC, those calculated from the 3.5- μm SPIREX/Abu continuum data and those obtained from

Table 4. The derived parameters of the two-component black-body fits to the SEDs for the southern globule (IRAS 10430-5931) and selected sources seen in the northern region (N1, N2, N3 and N4) as shown in Figs. 10 and 12. The parameters correspond to the temperature of the outer shell, T_{outer} , at the maximum radius, R_{max} , and the temperature of the inner shell, T_{inner} , at the minimum radius, R_{min} . Estimates of the luminosities (L_{TOT}), spectral types and IR spectral indices (α_{IR}) are also given.

Source	T_{outer} (K)	T_{inner} (K)	R_{min} (au)	R_{max} (au)	L_{TOT} ($10^4 L_{\odot}$)	Spectral Type	α_{IR}
IRAS 10430-5931	60 ± 4	430 ± 50	14 ± 3	$4\,760 \pm 100$	$1.3^b \pm 0.6$	B0–0.5	3.8
N1	87 ± 10	330 ± 30	39 ± 6	$1\,510 \pm 300$	6.2 ± 0.6	O8	5.8
N2	74 ± 6	290 ± 20	55 ± 10	$3\,930 \pm 200$	20 ± 6	O6–O6.5	7.1
N3	100 ± 15	2500^a	1.6 ± 0.8	640 ± 200	5.7 ± 0.7	O8.5	-1.7
N4	80 ± 10	380 ± 30	25 ± 10	$1\,440 \pm 200$	4.1 ± 0.5	O9–O9.5	4.6

^a lowest value for the temperature that fits the data given.

^b this value is consistent with the lower limit estimate given by Megeath et al. (1996).

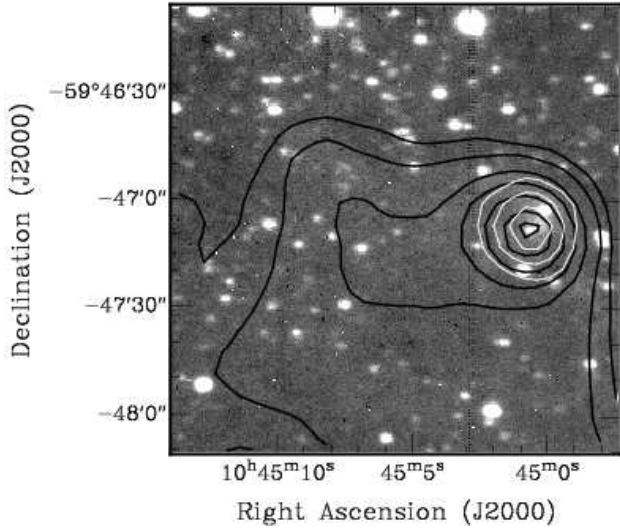


Figure 9. 2.2- μm (K-band) image in grey scale of the southern globule. Black contours represent 8- μm emission; 1.2, 1.5, 2, 2.5, 3, 3.5, $3.8 \times 10^{-5} \text{ W m}^{-2} \text{ sr}^{-1}$. White contours represent 21- μm emission; 4, 5, $6 \times 10^{-5} \text{ W m}^{-2} \text{ sr}^{-1}$.

Megeath et al. (1996) for the sources 1 and 3. For the 3.5- μm data, contamination from PAH emission at 3.29 μm was estimated to be approximately 30 per cent and was removed from the continuum flux value before placing it on the SED. Also included on the SED is the *IRAS* LRS for the source (thin line). The solid line is a two-component black-body fit to the data and represents the flux coming from two spherical shells of radius, R_{min} and R_{max} at corresponding temperatures T_{inner} and T_{outer} respectively. This model is a simple representation of the emission seen toward an obscured source whose radiation is absorbed and re-emitted by a surrounding spherical dust shell. The temperature of the dust shell decreases radially outwards, the temperatures T_{inner} and T_{outer} can be determined, along with the ratio of the angular sizes of the dust shells ($(R_{\text{min}}/R_{\text{max}})^2$) from this model. Using the known distance to the source, the luminosity and the derived temperatures, R_{min} and R_{max} can be determined. The parameters obtained from fits to this SED are given in Table 4.

Emission from PAH and absorption from silicate molecules is important to consider for this model. Contam-

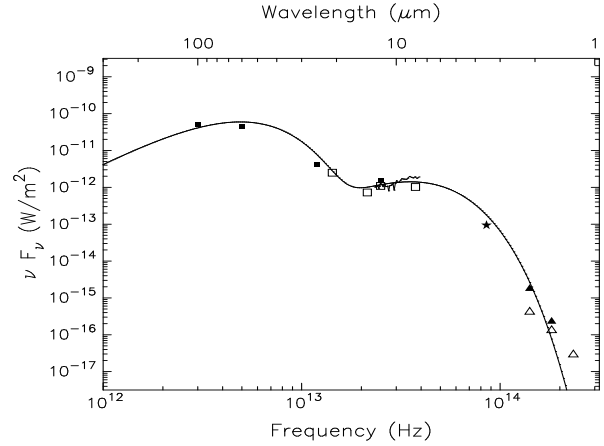
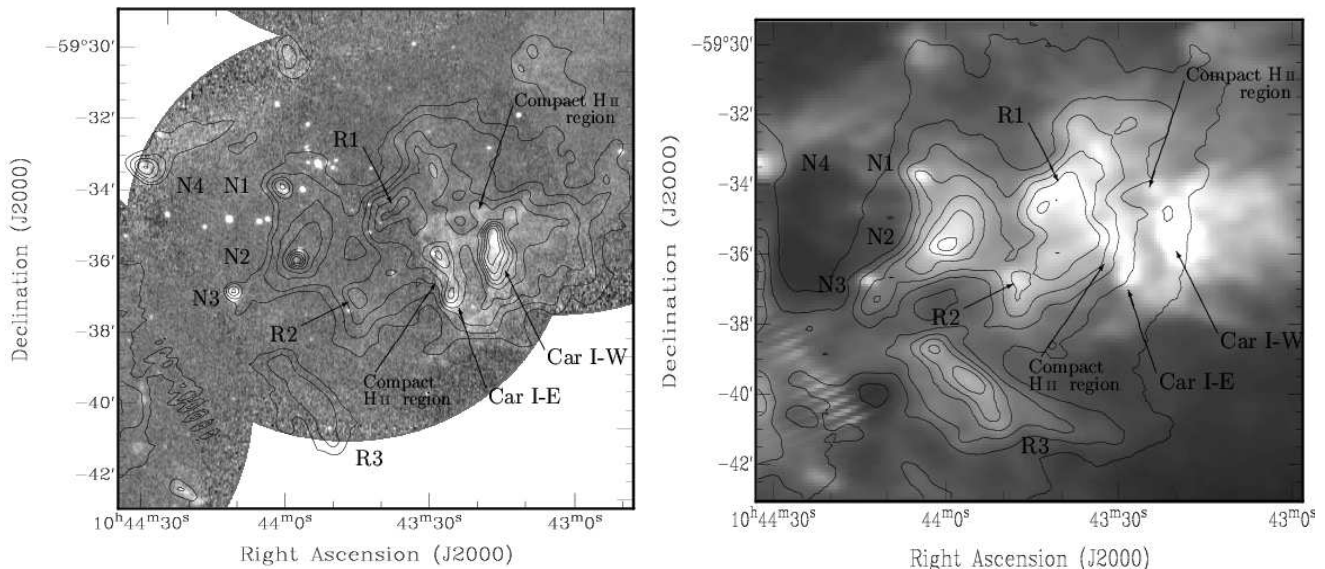


Figure 10. Continuum SED for the southern globule. Filled squares represent *IRAS* HIRAS data; open squares represent *MSX* data; the star represents 3.5- μm data from SPIREX/Abu; and the filled and open triangles represent the near-IR data from Megeath's source 1 and 3 respectively. The thin line represents the *IRAS* LRS spectrum for the globule, while the solid line represents the two-component black-body fit to the data (see Table 4).

ination from the former was removed from the data, but the latter remains in the SED. This is clearly seen as a dip in the spectrum, which is significant when attempting to determine the best fit. Although this is a simple fit to the temperatures and radii, this model allows us to obtain a first order estimation to the conditions within these regions.

The shape of the SED is consistent with a Class I low-mass YSO in the classification scheme of Lada (1987) (these classifications are only used in the current study to describe the shape of the SEDs as it is not clear if high-mass stars follow a similar evolutionary process). The shape of the SED is determined from the spectral index (α_{IR}), which is a measure of the slope of the SED between near- and mid-IR wavelengths (in this case between 2 and 21- μm). Although the SED rises in the far-IR, the exact region where the emission peaks is unclear from these data alone. It may be that the emission continues to increase into the sub-millimetre regime, thus corresponding to a lower outer temperature and higher total luminosity.

Megeath et al. (1996) also constructed a SED for this source, including only the *IRAS* and near-IR data points. From this limited information they put forward one possi-



(a) 3.29- μm emission in grey scale with contours of 8- μm emission. Levels are 2.7, 3.5, 4.5, 5.4, 6.5, 7.3, 8.1, 8.9, $9.7 \times 10^{-5} \text{ Wm}^{-2} \text{ sr}^{-1}$.

(b) 8- μm emission in grey scale with contours of 21- μm emission. Levels are 0.6, 1.1, 1.6, 2.1, 2.6, 3.1, $3.6 \times 10^{-4} \text{ Wm}^{-2} \text{ sr}^{-1}$.

Figure 11. The Northern Carina region. Several point sources are labelled on the image (N1, N2, N3 and N4), along with regions of diffuse emission (R1, R2, and R3), as well as the ionization fronts and compact H II regions identified by Brooks & Whiteoak (2001). The parallel stripes seen in the contours of (a) and the grey scale image of (b) are artifacts from diffractions of η Car. These images cover the same region as indicated in Fig. 1.

ble explanation for the shape of the SED suggesting that the globule contained an ultra-compact (UC) H II region. From the additional data shown here it appears this is indeed the case. The shape of the SED and the temperatures, radii and luminosities derived from it are all consistent with other UC H II regions identified (e.g. Walsh et al. 1999). The *MSX* colours (8–12 μm), (8–14 μm) and (8–21 μm) of 1.39 mag, 1.50 mag and 4.08 mag are also consistent with those properties of UC H II regions as determined from infrared models of the point-source sky (Wainscoat et al. 1992; Cohen 1993). Radio continuum images of the region however show no source coincident with the globule (Whiteoak 1994). The luminosity derived from the SED corresponds to a star of spectral type B0.5 (Panagia 1973). This most likely corresponds to Megeath’s source 1 (filled triangles in Fig. 10) as this source appears to be more consistent with the overall fit. In order to make a more confident distinction between the two sources however, higher resolution imaging is required.

3.4 Northern region

As noted earlier, the 3.29- μm emission in the northern part of the Carina Nebula extends over a large part of the northern molecular cloud and is brightest near the H II region Car I. Fig. 11(a) shows the 3.29- and 8- μm emission of this region in detail. The brightest 3.29- μm emission is concentrated at the edge of the molecular cloud, with faint diffuse emission seen extending across the region. In contrast, the 8- μm emission is much more diffuse and contains strong emission over the whole region, including those areas where there is faint 3.29- μm emission. Fig. 11(b) provides a com-

parison of the 8- and 21- μm emission. The emission structures coincide very closely, with the exception of the region containing strong 3.29- μm emission. Here there is almost no 21- μm emission and the bright 3.29- μm emission can be largely attributed to the PAH emission line. The regions labelled R1, R2 and R3 are the contrary. These regions show little 3.29- μm emission, with a strong coincidence between the 8- and 21- μm emission structures. This suggests the emission is from dust at these locations and most likely represents the back face of the molecular cloud.

3.4.1 The Car I H II region

Car I contains several ionization fronts arising from Tr 14 the most prominent being Car I-E and Car I-W (Whiteoak 1994; Brooks et al. 2001). Car I-E coincides with an optically bright-rimmed edge of the molecular cloud. Bright 3.29- μm emission also traces this edge and forms a series of linear ridges that point toward Tr 14. One of the southern ridges corresponds to a strong region of 8- μm emission (labelled as Car I-E in Fig. 11). Car I-W is situated further west and curves around a dense molecular clump. Bright 3.29- and 8- μm emission also trace this ionization front (labelled as Car I-W in Fig. 11). The absence of a strong coincidence between the 8- and 21- μm emission in both Car I-E and Car I-W confirms that the 8- μm emission can be attributed to PAH molecules. These results are consistent with a model proposed by Brooks et al. (2001) stating that Car I-E is interacting with the front face of the GMC and creating a PDR seen edge-on, while Car I-W is interacting with the back face and creating a second PDR seen face on.

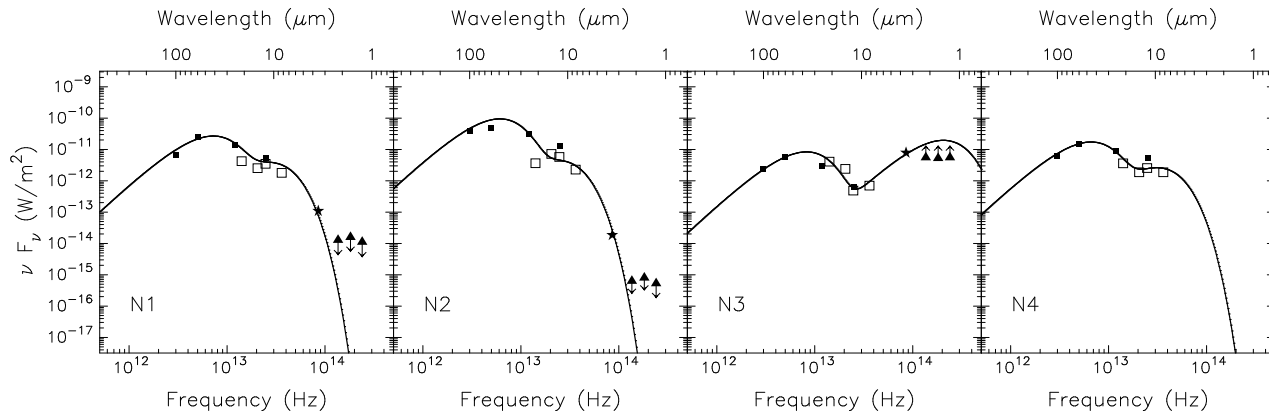


Figure 12. SEDs for sources seen in the northern region. Filled squares represent *IRAS* data; open squares represent *MSX* data; the star represents 3.5- μ m data from SPIREX/Abu; and filled triangles represent near-IR data from CASPIR. The solid line is the resulting two-component black-body fits to the data (see Table 4).

3.4.2 Point Sources and their SEDs

The two compact H II regions identified by Brooks et al. (2001) are located at the edges of the ionization fronts Car I-E and Car I-W (labelled in Fig. 11). The 8- μ m emission associated with Car I-E actually curves around the compact source located here. The second compact H II region associated with the edge of Car I-W further to the north, shows a coincidence with 3.29- μ m emission, faint 8- μ m emission but very little 21- μ m emission.

Several new point sources are evident in the 8- μ m image (labelled N1, N2, N3 and N4) and are located on the edges of a small region completely devoid of all IR emission. The sources N1 and N2 correspond to extended sources in the 3.29- μ m image, with differing amounts of heated dust extending around them (as traced by the 21- μ m emission). The source N3 corresponds to a strong point source in 3.29- μ m emission, with little 21- μ m emission. A peak in 21- μ m emission exists slightly offset from this position, however it is not clear if this feature is related to the 8- μ m source. The source N4 shows a strong coincidence between the 3.29- and 8- μ m structures, with little 21- μ m emission associated with it, suggesting the emission is from PAH molecules.

The spatial offsets between the 8- and 21- μ m peaks of these sources might be attributable to contamination of the 21- μ m contours by a strong 22- μ m dust emission feature. If this feature exists across the whole Car I region and is excited by either Tr 14 or η Car, then the amount of contamination determined from the Chan & Onaka spectra will only serve as a lower limit (as estimated in section 2.2). The point sources identified here are located closer to both possible sources than the positions at which the spectra were taken and thus would be more likely to have a higher amount of the 22- μ m dust feature underlying the overall emission. Without spectra nearer to the individual point sources, it is difficult to estimate the contamination seen in the 21- μ m band due to the underlying 22- μ m dust emission feature.

The SEDs for the point sources N1, N2, N3 and N4 are shown in Fig. 12. Due to the complexity and confusion in this region, several of these sources contained flags in the *MSX* PSC1.2 indicating the emission was a lower limit; a result of their extended nature. For these cases, the flux over the region approximating the 8- μ m peak was estimated and

a nearby background removed. To confirm that this method derived acceptable flux estimates, the flux was also measured for the sources in the bands where there was data in the PSC1.2. The estimation of the flux was, in the worst case, a factor of 2 larger than the correct value. This method was also used to estimate the *IRAS* fluxes at these locations. Several *IRAS* sources exist in this region, but none were found to be consistent with the 8- μ m point sources. The effects of contamination from 3.29- μ m PAH emission for the continuum fluxes obtained at 3.5 μ m were also estimated for these sources (30 per cent for N1, 5 per cent for N2 and 1 per cent for N3) and were removed from the flux value before placing the point on the SED. The coincidence between the *MSX* and *IRAS* points near 21- μ m for the sources N3 and N4 suggest the possible contamination from the 22- μ m dust emission feature is small. However, for the source N1 and N2, the differing flux values could possibly result from a strong 22- μ m dust emission feature seen near these sources. A quantitative estimate of such contamination however is difficult with the current data set.

Near-IR images of the sources N1 and N2 reveal extended diffuse emission. The fluxes shown in the SEDs for these wavebands are representations of the emission at these points and are upper limits to any source that may be associated with the 8- μ m peak. For N3 there exists a strong source in the near-IR images, saturating in our images, hence the flux plotted on the SED for this source represents a lower limit to the actual flux. The source N4 was outside our observed regions, but shows a very red and extended region in 2MASS[¶] three colour images of the region, consistent with the SED fit at these wavelengths.

The solid lines in these plots represent the two-component black-body fits as described in section 3.3.2. The parameters from these simple fits are given in Table 4. The sources N1, N2 and N4 have similar properties to the SED for the southern globule; they peak in the far-IR, correspond to similar temperatures and radii, have $\alpha_{\text{IR}} > 0$ and luminosities that correspond to early type stars (in this case O6–O9.5). Most likely these sources correspond to UC H II

[¶] For more information about the 2MASS project and database, see <http://www.ipac.caltech.edu/2mass/index.html>

regions. Source N3 however displays the same features in the far-IR as the other sources but shows remarkably different characteristics in the thermal- and near-IR regimes. This results in an α_{IR} of -1.7, similar in shape to a Class II SED and thus more evolved than the other sources in the region. These objects are thought to represent young stars surrounded by a circumstellar disc of material (Lada 1987). The fact that there is emission in the far-IR suggests that cool dust still exists around this source and is therefore consistent with this picture.

4 CONCLUSIONS

We have obtained high-resolution, wide-field 3.29- μm emission images across the Carina Nebula in order to trace the PDRs thought to be widespread in regions of massive star formation. Combined with *MSX* 8–21 μm data, *CASPIR* 2.2- μm data and *SEST* molecular line data, these images emphasize the three different environments of the Carina Nebula: the Keyhole, southern and northern molecular cloud regions.

4.1 Keyhole region

The Keyhole region contains many of the discrete clumps identified in our images, several of which have been studied previously. Two additional clumps were identified via their 3.29- μm PAH emission and mapped in $^{12}\text{CO}(2-1)$ and $^{12}\text{CO}(1-0)$. Combined with published data for the other clumps in the region, it is clear that all the molecular material in this region is exposed to the same intense FUV radiation. The high $^{12}\text{CO}(2-1)$ and $(1-0)$ line ratios, as well as significantly higher Virial masses compared to the LTE mass estimates, suggests that all the clumps are externally heated with PDRs on their surfaces and supported by external pressure. This is consistent with suggestions that the clumps are photo-evaporating and represent the swept-up remains of the molecular material from which η Car formed. The clumps also follow the geometrical model developed by Brooks et al. (2000) relating their optical appearance, PAH emission structures and velocities to their location within the region and with respect to η Car. While these new clumps are consistent with the above-mentioned properties, there are certain differences that set them apart. Both of these structures have higher PAH fluxes and larger sizes relative to the other clumps in the region. This suggests that the photo-evaporation process may be slower for these clumps, a direct consequence of their further displacement from η Car.

4.2 Southern region

Toward the southern region the images reveal an externally heated globule with a correspondence between strong 3.29-, 8- and 21- μm emission. The morphology of the globule suggests that the winds and FUV radiation from η Car and Tr 16 may be responsible for carving the molecular material around a dense compact region, penetrating into the molecular cloud and forming a PDR on its surface. The location is also consistent with IRAS 10430-5931 and four sources displaying anomalous near-IR colours. By comparison with

the locations of the near-IR sources and the mid-IR data, we were able to eliminate two of these sources as producing the observed fluxes. The SED shows a peak in the far-IR, falling off at shorter wavelengths. Through the use of a two-component black-body fit to this SED we have tentatively identified the emission as coming from a single source, most likely corresponding to an UC H II region.

4.3 Northern region

The northern region displays more varied phenomena than either the Keyhole or southern regions. Here, we see regions of strong PAH emission and regions containing heated dust, both separately and inter-mixed. The diffuse PAH emission we see is consistent with the edge of the molecular cloud and with the strong ionization fronts Car I-E and Car I-W. The coincidence between the 3.29- and 8- μm data at these locations confirms the existence of PDRs at these interfaces.

Several strong 8- μm point sources are evident in this region and are located on the edge of a small region completely devoid of extended 3.29-, 8- and 21- μm emission. SEDs for these sources and two-component black-body model fits to these data suggest three of the four sources are Class I protostars. The fourth source has a different SED, peaking in the near-IR/optical regime with significant far-IR emission. This SED is characteristic of a more evolved Class II protostar, containing a young star surrounded by a circumstellar disc (rather than completely embedded).

4.4 Ongoing star formation in the Carina Nebula?

From the data presented here it is clear that star formation within the Carina Nebula has not been completely halted by the clusters of young massive stars. This supports the changing view that the Carina Nebula contains active star formation, contrary to previous conclusions. The northern region was found to contain more sites of massive star formation compared to the southern and Keyhole regions. All young stars identified are associated with UC H II regions and are possibly a result of triggered star formation. The four sources identified in the northern region for instance, all lie on the edges of a small cavity devoid of IR emission.

The differing environments of these three regions contributes significantly to the star formation activity seen within them. The Keyhole region shows the effects of such a close proximity to η Car, the environment being too harsh for any star formation activity. It may be however, that the massive stellar members of Tr 16 including η Car, are contributing to star formation at the edge of the southern molecular cloud. It appears as if the winds and radiation from these massive stars may be disrupting the molecular cloud and inducing star formation within a globule on the edge. The environment in the northern region produced by Tr 14 is also extremely disruptive on the surrounding GMC. The location and identification of the star formation activity, PDRs and greater amounts of heated dust in this region is consistent with a younger age for Tr 14 compared to Tr 16 and the southern molecular cloud. Thus the environment in the Keyhole and southern regions may represent a future state for the northern region.

ACKNOWLEDGMENTS

We would like to thank Andrew Walsh and Angie Schultz for invaluable discussions, colleagues from CARA for their support in operating the facilities at the South Pole, in particular Charley Kaminski for taking the SPIREX/Abu data. We acknowledge the support of the Australian Research Council and travel funding obtained through ANSTO. MC thanks NASA for supporting this work through its Long Term Space Astrophysics programme, under grant NAG5-7936 with UC Berkeley.

REFERENCES

- Allamandola L. J., Tielens A. G. G. M., Barker J. R., 1985, *ApJ*, 290, L25
- Allamandola L. J., Tielens A. G. G. M., Barker J. R., 1989, *ApJS*, 71, 733
- Arendt R., Dwek E., Moseley S., 1999, *ApJ*, 521, 234
- Brooks K. J., 2000, Ph.D. thesis, University of New South Wales, Australia
- Brooks K. J., Burton M. G., Rathborne J. M., Ashley M. C. B., Storey J. W. V. S., 2000, *MNRAS*, 319, 95
- Brooks K. J., Storey J. W. V., Whiteoak J. B., 2001, *MNRAS*, in press
- Brooks K. J., Whiteoak J. B., Storey J. W. V., 1998, *Proc. Astron. Soc. Aust.*, 15(2), 202
- Buisson G., Desbats L., Duvert G., Forveille T., Gras R., Guilleoteau S., Luca R., Valiron P., 1999, GILDAS – An introduction to Grenoble and Line Data Analysis System, see <http://iram.fr/GS/gildas.html>
- Burton M. G. et al., 2000, *ApJ*, 542, 359
- Castets A., Duvert G., Dutrey A., Bally J., Langer W. D., Wilson R. W., 1990, *A&A*, 234, 469
- Chan K. W., Onaka T., 2000, *ApJ*, 533, L33
- Cohen M., 1993, *AJ*, 105, 2860
- Cohen M., Allamandola L. J., Tielens A. G. G. M., Bregman J., Simpson J. P., Witteborn F. C., Wooden D., Rank D. M., 1986, *ApJ*, 302, 737
- Cohen M., Tielens A. G. G. M., Bregman J., Witteborn F. C., Rank D. M., Allamandola L. J., Wooden D., de Muizon M., 1989, *ApJ*, 341, 246
- Cohen M., Walker R. G., Witteborn F. C., 1992, *AJ*, 104, 2030
- Cox P., 1995, *RevMexAA (Serie de Conferencias)*, 2, 105
- Cox P., Bronfman L., 1995, *A&A*, 299, 583
- de Graauw T., Lidholm S., Fitton B., Beckman J., Israel F. P., Nieuwenhuijzen H., Vermue J., 1981, *A&A*, 102, 257
- Egan M. P., Shipman R. F., Price S. D., Carey S. J., Clark F. O., Cohen M., 1998, *ApJ*, 494, L199
- Fowler A. M. et al., 1998, *Proc. SPIE*, 3354, 1170
- Gardner F. F., Morimoto M., 1968, *ApJ*, 21, 881
- Geballe T. R., Joblin C., d'Hendecourt L., Jourdain de Muizon M., Tielens A. G. G. M., Léger A., 1994, *ApJ*, 434, L15
- Genzel R., Harris A. I., Stutzki J., Jaffe D. T., 1988, *ApJ*, 332, 1049
- Gooch R., 1996, in Jacoby G. H., Barnes J., ed, *Astronomical Data Analysis Software and Systems V*, Vol. 101. ASP Conference Series, San Francisco, p. 80
- Grabelsky D. A., Cohen R. S., Bronfman L., Thaddeus P., 1988, *ApJ*, 331, 181
- Hasegawa T., 1996, in Latter W. B., Radford S. J. E., Jewell P. R., Mangum J. G., Bally J., ed, *CO: Twenty-five Years of Millimeter-Wave Spectroscopy - Proceedings of the 170th Symposium of the IAU*. Kluwer, Dordrecht, p. 39
- Hereld M., Rauscher B. J., Harper D. A., Pernic R. J., 1990, *Proc. SPIE*, 1235, 43
- Hollenbach D., Tielens A. G. G. M., 1999, *Rev Mod Phys*, 71, 173
- Joblin C., Tielens A. G. G. M., Allamandola L. J., Léger A., d'Hendecourt L., Geballe T. R., Boissel P., 1995, *Planet. Space Sci.*, 43, 1189
- Jones A., Frey V., Verstraete L., Cox P., Demyk K., 1999, in Cox P., Kessler M., ed, *The Universe as Seen by ISO*. ESA SP-427; Noordwijk: ESA, p. 679
- Lada C., 1987, in Peimbert M., Jugaku J., ed, *IAU Symp.* 115, *Star Forming Regions*. Kluwer, Dordrecht, p. 1
- Léger A., Puget J. L., 1984, *A&A*, 137, L5
- McGregor P., Hart J., Downing M., Hoadley D., Bloxham G., 1994, *Experimental Astronomy*, 3, 139
- McGregor P. J., 1995, CASPIR data reduction routines, see <http://msowwww.anu.edu.au/observing/docs/manual/manual.html>
- Megeath S. T., Cox P., Bronfman L., Roelfsema P. R., 1996, *A&A*, 305, 296
- Meixner M., Haas M. R., Tielens A. G. G. M., Erickson E. F., Werner M., 1992, *ApJ*, 390, 499
- Mill J. D., O'Neil R. R., Price S., Romick G. J., Uy O. M., Gaposchkin E. M., 1994, *J. Spacecraft Rockets*, 31, 900
- Moutou C., Verstraete L., Léger A., Sellgren K., Schmidt W., 2000, *A&A*, 354, L17
- Panagia N., 1973, *ApJ*, 78, 929
- Price S. D., Egan M. P., Carey S. J., Mizuno D., Kuchar T., 2001, *AJ*, 121, 2819
- Retallack D. S., 1983, *MNRAS*, 204, 669
- Sakamoto S., Hayashi M., Hasegawa T., Handa T., Oka T., 1994, *ApJ*, 425, 641
- Schneider N., Stutzki J., Winnewisser G., Poglitsch A., Madden S., 1998, *A&A*, 338, 262
- Scoville N. Z., Sargent A. I., Sanders D. B., Soifer B. T., 1991, *ApJ*, 366, L5
- Sellgren K., Werner M. W., Dinerstein H. L., 1983, *ApJ*, 217, L13
- Smith N., Egan M. P., Carey S., Price S. D., Morse J. A., Price P. A., 2000, *ApJ*, 532, L145
- Stutzki J., Stacey G. J., Genzel R., Harris A. I., Jaffe D. T., Lugten J. B., 1988, *ApJ*, 332, 379
- Tauber J. A., Lis D. C., Keene J., Schilke P., Buettgenbach T. H., 1995, *A&A*, 297, 567
- Tovmassian H. M., 1995, *RevMexAA (Serie de Conferencias)*, 2, 83
- Ulich B. L., Haas R. W., 1976, *ApJ*, 30, 247
- Verstraete L. et al., 2001, *A&A*, 372, 981
- Wainscoat R. J., Cohen M., Volk K., Walker H. J., Schwartz D. E., 1992, *ApJS*, 83, 111
- Walborn N. R., 1995, *RevMexAA (Serie de Conferencias)*, 2, 51
- Walsh A. J., Burton M. G., Hyland A. R., Robinson G., 1999, *MNRAS*, 309, 905
- Whiteoak J. B., Otrupcek R. E., 1984, *Proc. Astron. Soc. Aust.*, 5(4), 552
- Whiteoak J. B. Z., 1994, *ApJ*, 429, 225